Experimental investigation of thermal conductivity during aging of nanoporous sintered silver

A Sghuri, Y Billaud, L Signor, D Saury, X Milhet

cite as: A. Sghuri, Y. Billaud, L. Signor, D. Saury, X. Milhet, « Experimental investigation of thermal conductivity during aging of nanoporous sintered silver », Acta Materialia, Volume 257 (September), 119109, 2023.
DOI: 10.1016/j.actamat.2023.119109

Experimental investigation of thermal conductivity during aging of nanoporous sintered silver

A. Sghuri, Y. Billaud, L. Signor, D. Saury, X. Milhet

Institut Pprime ◇ UPR CNRS 3346 ◇ ENSMA ◇ Université de Poitiers, 1 Avenue Clément Ader,

F-86961 Chasseneuil-Futuroscope, France

E-mail: xavier.milhet@ensma.fr.

Abstract : Silver (Ag) paste sintering is used as a die-bonding technology for the next generation of power electronic modules as Ag offers a high melting temperature as well as excellent thermal and electrical conductivities. Ag paste sintering is performed using specific conditions depending on the type of paste and the users' specifications (temperature, time, pressure), ending up in a porous joint. As a result, the properties of those joints are heavily influenced by their densities (i.e. porosity). Despite the numerous studies reported in the literature, the relationship between the density of the joint and its thermal conductivity remains an issue since access to the density of an embedded thin joint is very challenging. Furthermore, little is known on the evolution of the thermal conductivity in operating conditions. In this study, these issues were investigated by developing self-standing specimens with microstructures representative of those of real joints. In order to study a wide range of porosity, sintering was performed using a single time/temperature under various pressures. The thermal conductivity was measured using 3D flash method, consisting in applying a short non-uniform laser excitation on the surface of the sample, leading to three-dimensional heat transfer. The relationship between porosity and thermal conductivity is established for the as-sintered state and after aging up to 500 h at temperatures ranging from 150°C to 350°C and is compared to existing models. The evolution of the thermal properties during thermal aging is discussed considering both the elaboration conditions and the microstructure evolution.

Keywords : Porous silver, sintering, thermal conductivity, aging, microstructure, 3D flash, inverse method.

1. Introduction

Silver (Ag) paste sintering is used as a die-bonding technology for the next generation of power electronic modules as Ag offers a high melting temperature as well as excellent thermal and electrical conductivities. Ag paste sintering is performed using specific conditions depending on the type of paste and the users' specifications (low temperature with or without applied pressure for a short time), ending up in a porous joint. As a result, the properties of those joints are heavily influenced by their densities (i.e. porosity). Overall, the reliability of sintered Ag joints depends on four factors: i) the silver paste in terms of particle size, type of solvents and general formulation, and ii) the sintering process that affects both the porosity and grain size, iii) the design in terms of thickness of the Ag joint and its interfaces with the substrate and the device, and iv) the effect of thermal aging of sintered Ag and the interfaces within the electronic system. All of these factors are critical for the lifespan of the electronic device. Actually, sintered Ag plays a key role for the heat dissipation within the system but the influence of the time exposure at temperatures close to in-service conditions on the thermal conductivity is not well documented in the literature. This must be addressed since it may cause a drastic reliability issue if aging causes a loss of heat dissipation resulting in overheating within the power module. While the relationship between density and mechanical properties (Young Modulus, tensile properties) of sintered Ag is now relatively well established, the thermal properties reported in the literature are very scattered [1–11]. The thermal conductivity of a porous material can be estimated using Eq. (1).

$$\lambda = \alpha \cdot \rho \cdot c \tag{1}$$

Where λ is the thermal conductivity, α is the thermal diffusivity, ρ is the density and c is the specific heat

capacity. The accurate measurement of both the density (i.e. porosity) and heat capacity of the porous material is then a key factor for estimating their thermal conductivity. The role of the sintering parameters for various silver paste type (micropaste or nanopaste) on the microstructure and the thermal properties is an active research topic. The specimen configuration (pure sintered Ag, Ag sintered on a substrate or Ag embedded within a complex stack of known materials) depends on the measurement method used. Several studies report the effect of various parameters, e.g. particle size, time, temperature and pressure, on the thermal conductivity of sintered Ag [9, 12–19]. For example, Wereszczak et al. studied different types of micrometric pastes and showed the influence of sintering time and temperature on the thermal conductivity of relatively large sintered Ag specimens [16]. They observed that the longer the sintering time and the higher the sintering temperature, the greater the density and therefore the greater the thermal conductivity. Ras et al. showed that the sintering pressure is a first order parameter compared to the sintering temperature for the thermal conductivity [15]. Other studies showed that sintering a paste with a bimodal particle size distribution gives a denser joint resulting in a higher thermal conductivity [2, 6]. Furthermore, Suganuma al. also showed that a relatively good thermal conductivity can be obtained even when sintering is performed at low temperature without applying a stress if the sintering time is long enough [2]. Realistic configurations, where the Ag joint is embedded within a stack of different materials, were used by Ordonez-Miranda et al. to investigate the dependence of sintering parameters on thermal conductivity of the joint [13]. They showed that: i) the density of the embedded sintered layer is difficult to estimate (in general, it is performed by surface analysis using SEM images), ii) the heat capacity of the stack requires sintering a separate Ag joint in the same conditions or, more simply, using the heat capacity of bulk Ag and iii) even if the thermal conductivities of every other materials within the stack, but sintered Ag, are well known, the presence of interfaces, with unknown thermal resistances, increases the scatter of the measurements. In addition to the sintering parameters, thermal aging was shown to affect the thermal properties of sintered Ag. Qin et al. proposed a model to study the influence of microstructures on thermal conductivity based on an evolution of

the density during thermal aging reported previously [20, 21]. They showed that the conductivity increases after a short thermal aging time, then decreases for longer aging time. They suggest that this evolution is controlled by: i) an improvement of the densification at the begining of aging e.g. a decrease of the overall porosity of the Ag joint thanks to the short thermal aging (the better density helps with the heat dissipation hence a better thermal conductivity) followed by ii) the decrease of the thermal conductivity because of a development of damages, resulting from the increasing the aging time. These aging damages are assumed to promote an increase of the overall porosity of the joint.

Overall, while many studies report the influence of the elaborating conditions on the thermal conductivities, the intrinsic relationship between porosity (density) and thermal conductivity is still not well established for sintered Ag and the data are scattered. Furthermore, other microstructure parameters may have an impact on the thermal conductivity and should be also considered [22–26]. The present study aims at addressing this issue using an original experimental approach for which specific sintered Ag specimens are elaborated with different sintering parameters to obtain a wide range of densities. The evolution of the thermal diffusivities during thermal aging, up to 500 h over a wide temperature range, is also investigated considering the evolution of the microstructure.

2. Experimental procedure

2.1. Material and sintering process

Self-standing rectangular specimens (50×50 mm^2) were prepared using the McDermidAlpha Argomax® 8020 silver paste. The sintering process followed the procedure described in [3]. This elaboration method includes a first step dedicated to evaporating the solvent at room temperature under vaccum prior to sintering at 270 °C. Both the time required for solvent evaporation and the sintering temperature were determined by Differential Scanning Calorimetry (DSC, Q20, TA Instruments) [3]. After solvent evaporation, the specimens were sintered for 5 min at 270 °C under different stresses (0, 2, 5 and

10 MPa) in air in order to obtain a wide range of densities. During sintering, the load was applied along the z-axis as shown in Fig.1. The thicknesses of the specimens range from 0.4 to 1.40 mm depending on the applied stress. The density of each specimen was carefully determined from the classical mass to volume ratio using a high-precision Sartorius MZ1 scale (with a resolution better than 10 mg) and an optical profilometer with an accuracy better than 1 µm. The relative porosity p of each specimen was obtained from the measured density ρ using Eq. (2)

$$p = 1 - \rho/\rho_0 \tag{2}$$

Where $\rho_0 = 10.5\ g.cm^{-3}$ is the density of dense Ag. As a result, the pore fraction was estimated to lie within the range 25% to 75% $\pm$ 2% depending on the sintering conditions. The heat capacity of sintered Ag was measured for each elaboration condition using DSC Modulated mode with a standard deviation of 5%. Isothermal aging was performed at 150, 250 and 350 °C under primary vacuum for 0, 50, 200 and 500 h. Primary vacuum was chosen to limit the oxidation of Ag during aging. Overall, 48 conditions, including as-sintered state and aging were explored. Grain size evolution with aging time was monitored using dedicated samples with dimensions of $10 \times 10 \times 0.4\ mm^3$ sintered at 2 MPa and 10 MPa. They were aged simultaneously to the specimens dedicated to the thermal conductivity measurements. Grain size and pore fraction were measured using Back Scattered Electron imaging (BSE) in a JEOL 7000 field emission gun scanning electron microscopy (FEG-SEM) operating at $20kV$. Before and after each aging step, a careful surface preparation, including a final step of chemo-mechanical polishing, was performed. The grain size was estimated using ImageJ software. In particular, the average grain size was obtained by analyzing over 400 grains distributed in 3 different zones for each specimen. In order to evaluate the behavior of the density, grain size throughout aging, the standard oneway analysis of variance (ANOVA) followed by Tukey's test was used (with a significance level for rejection of null hypothesis at 5% means comparison). This analysis was performed using OriginPro®.

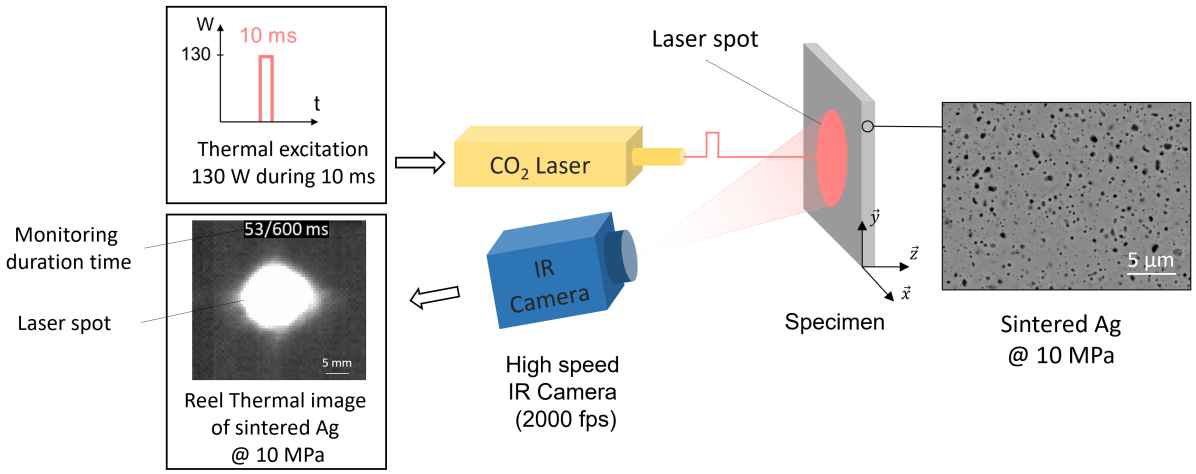

Fig. 1. Schematic diagram of flash 3D method used in this study.

2.2. *Thermal conductivity measurement*

The thermal conductivity was obtained by 3D flash method using the following procedure: (i) experimental measurements providing the temperature fields at the surface of the sample Fig. 1, (ii) mathematical modelling mimicking the experiment, and (iii) an estimation procedure (i.e. an estimator) coupling the experimental and model results Fig. 2.

The experimental setup is similar to that described by [27]: the specimen is heated with a localized and non-uniform thermal excitation obtained using a CO2 laser (DIAMOND GEM-Series by coherent, 10.6 µm). The pulsed excitation duration time is set at 10^{-3} s delivering a maximal excitation power of $130W$. The surface temperature evolution is continuously measured using an infrared (IR) camera (FLIR SC7000) set at a frequency of 1950 Hz and a spatial resolution of 80×64 pixels. In the case of highly conductive materials i.e. bulk metals, the monitoring duration time is set at 0.6 s, corresponding to 1200 frames. Prior to the measurements, the surface of each specimen was sprayed with a thin layer of black matte paint (thickness < 10 µm) in order to increase the absorption of the pulsed laser beam without altering the measurements. The maximum diameter after the initial excitation by the laser reaches 30 mm during the heat transfer, which is well below the lateral dimensions of the specimens.

In the model, the heat transfer inside the samples is assumed to behave according to the 3D equation of heat conduction in Cartesian geometry. The heat conduction equation and the boundary conditions are:

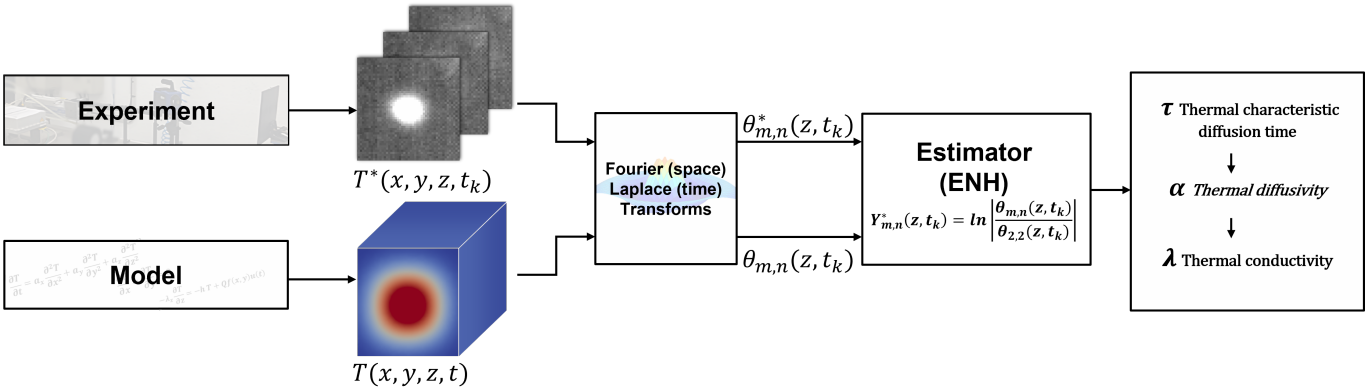

Fig. 2. Estimation procedure associated with the 3D flash method.

$$\rho C\frac{\partial T}{\partial t} = \lambda_x\frac{\partial^2 T}{\partial x^2} + \lambda_y\frac{\partial^2 T}{\partial y^2} + \lambda_z\frac{\partial^2 T}{\partial z^2} \tag{3}$$

$$-\lambda_x\frac{\partial T}{\partial x} = 0 \; for \; x = 0 \; and \; x = l_x \tag{4}$$

$$-\lambda_y\frac{\partial T}{\partial y} = 0 \; for \; y = 0 \; and \; y = l_y \tag{5}$$

$$-\lambda_z\frac{\partial T}{\partial z} = -hT + \phi(x,y,t) \; for \; z = 0 \tag{6}$$

$$\lambda_z\frac{\partial T}{\partial z} = hT \; for \; z = l_z \tag{7}$$

$$T = 0 \; for \; t = 0 \tag{8}$$

where $\phi(x,y,t)$ is the heat flux absorbed by the sample. A Laplace transform in time and a cosine Fourier transform in space is applied to solve the system. The temperature field $T(x,y,z,t)$ is then projected onto the basis $X_m(x) = \cos(\alpha_m x)$ and $Y_n(y) = \cos(\beta_n y)$ leading to the harmonics temperature field $\theta(\alpha_m, \beta_n, z, p)$.

$$\theta(\alpha_m,\beta_n,z,p)=\int_0^{\infty}\int_0^{l_x}\int_0^{l_y}T(x,y,z,t)X_m(x)Y_n(y)\cdot e^{-pt}dtdxdy \tag{9}$$

where α_m,β_n are pulsations along-x and y-axis associated with harmonic (m,n) and p is Laplace variable. On the top of the sample, at $z=0$, and for a Dirac pulse type excitation ($u(p)=\int_0^{\infty}\delta(t)\cdot e^{-pt}\cdot dt=1$), the harmonics temperature field evolution [28] is obtained by:

$$\theta(\alpha_m,\beta_n,z,t)=QR_{m,n}\left[2\sum_{k=1}^{\infty}\frac{u_kZ_kz}{u_k^2+H^2+2H}e^{-\tau_z u_k^2 t}\right]\cdot e^{-(\tau_x m^2+\tau_y n^2)\pi^2 t} \tag{10}$$

where τ_x, τ_y and τ_z are the thermal characteristic diffusion times along the 3 axes and $R_{m,n}$ the shape function describing the spatial distribution of the excitation energy projected in the same basis as the analytical solution. The parameters u_k (solution of the transcendent equation), H (the Biot number) and $Z_k(z)=u_kcos(u_kz/l_z)+Hsin(u_kz/l_z)$ do not affect the estimation thanks to the procedure hereafter. The estimator, known as ENH (Estimation by Normalization of Harmonics), used in this study was proposed by [29–32] and improved by [28]. ENH consists in dividing the measurement by a reference harmonic, in this work $\theta_{2,2}$, to transform the nonlinear inverse problem into a linear inverse problem relatively to the characteristic diffusion times in the excitation plane (τ_x and τ_y). After linearization, both the characteristic diffusion times components and the parameters associated to the non-uniform excitation are estimated simultaneously.

The linearized model outputs $Y_{m,n}(z,t_k)$ are then introduced:

$$Y_{m,n}(z,t_k)=\ln\left|\frac{\theta_{m,n}(z,t_k)}{\theta_{2,2}(z,t_k)}\right| \tag{11}$$

with t_k the acquisition time for each frame k. Substituting Eq. (10) in Eq. (11) gives:

$$Y_{m,n}(z,t_k)=-(\tau_x m^2+\tau_y n^2)\pi^2 t_k+\ln\left|\frac{R_{m,n}(z,t_k)}{R_{2,2}(z,t_k)}\right| \tag{12}$$

Eq. (12) shows that the model outputs $Y_{m,n}(z,t_k)$ are linear with respect to time for every harmonic (m,n).

The odd harmonics (i.e. whose values of m and/or n are odd), are three order of magnitude smaller than the even harmonics, due to the symmetrical nature of the excitation. The odd harmonics are then not used in the estimation procedure. The harmonics exploited for the identification procedure are the even and low frequencies harmonics, $Y_{m,n}$ where m,n combination corresponds to $[0,2,...,6]\times[0,2,...,6]$, leading to a system of $4\times 4=16$ equations. In-plane characteristic diffusion times τ_x and τ_y are estimated simultaneously in order to minimize the system error. Both temperature fields were found identical when measured in the front surface (where the laser flash is sent) and the back surface (corresponding to a measure after that the heat generated in the front surface diffuses along the z-axis). The slight discrepancy between the values in τ_x and τ_y directions lies within the standard deviation. Therefore, it is assumed that the thermal behavior of sintered Ag is isotropic. In the following, the value of the characteristic diffusion time τ corresponds to the arithmetic average of τ_x and τ_y.

The thermal diffusivity is then calculated $\alpha = l_x \cdot l_y \cdot \tau$ to finally estimate the thermal conductivity using the Eq. (1).

2.3. Calibration of the setup measurement with standard materials

In order to assess the reliability of the approach, measurements of the thermal conductivities were first performed on 3 well-known standard bulk materials with high conductivities i.e. aluminum (Al, density 2.70 $g.cm^{-3}$, purity 99.95%), copper (Cu, density 8.91 $g.cm^{-3}$, purity 99.95%) and finally silver (Ag, density 10.49 $g.cm^{-3}$, purity 99.95%). The results are listed in Table 1. 20 Measurements were performed for each bulk specimen using the same set of parameters to estimate the error and the variance of the outcome results. Actually, these uncertainties may derive from all the experimental steps (experimental measurements, calibration laws, model resolution and estimation method) [28, 33–35].

As seen in Table 1, the results agree very well with those found in the literature [36–38]. For each of the sintered Ag specimens, the behavior of thermal conductivities during aging was scrutinized using the

	Thermal conductivity ($W.m^{-1}.K^{-1}$)	
	This study	References [31-33]
Ag	426.7 ± 25	426 - 433
Cu	398.9 ± 24	386 - 401
Al	236.7 ± 14	237 - 239

TABLE 1. Measured thermal conductivities of pure and dense reference silver, copper and aluminum samples.

Sintering pressure (MPa)	0	2	5	10
Density ($g \cdot cm^{-3}$) $\pm 2\%$	2.85	5.41	6.65	7.74
Heat capacity ($J \cdot Kg^{-1} \cdot K^{-1}$) $\pm 5\%$	600	347	305	287

TABLE 2. Density and heat capacity as function of sintering pressure

standard oneway analysis of variance (ANOVA) followed by Tukey's test with the same significance level (5% means comparison).

3. Results

3.1. Thermal conductivity as a function of the density

As mentioned previously, the thermal conductivity is measured using Eq. (1). The results of the specific heat capacities are listed in Table 2. Fig. 3 plots the thermal conductivity of as-sintered silver as function of relative porosity. As expected, the thermal conductivity improves as the material density increases. It can be pointed out that on the porosity range studied (from 25% to 75% $\pm$ 2%), the thermal conductivity decreases by a factor of 4, from 222 to 66 W/m.K respectively.

Fig. 3 also plots the evolution of the thermal conductivities as a function of the porosity and pore shape (spherical, cylindrical and pancake-shaped) using the model developed by Ordonez-Miranda et al. [13]. This model is based on the differential effective medium theory and provides a simple analytical description considering the pores as ellipsoidal voids of different sizes randomly distributed and oriented in an Ag matrix. Following this work, the effective thermal conductivity for different pore shapes and porosity is calculated as follows:

$$\lambda_{eff} = \lambda_0 (1-p)^n \tag{13}$$

with $n = \frac{3L+1}{6L(1-L)}$ and

$$L = \frac{\xi^2}{2(\xi^2-1)} \begin{cases} 1 - \frac{\cosh^{-1}(\xi)}{\xi(\xi^2-1)^{1/2}}, & \text{for } \xi > 1 \\ \\ 1 + \frac{\cos^{-1}(\xi)}{\xi(1-\xi^2)^{1/2}}, & \text{for } \xi < 1 \end{cases} \tag{14}$$

with λ_0 the thermal conductivity of the matrix and $\xi = a/b$ the aspect ratio of the ellipsoidal pores of semi-axis a and b. According to Eq. (13), the thermal conductivity λ is driven by the pore shape and decreases according to a power law controlled by the parameter n. The values of n are 3/2, 5/3 and ∞ for spherical, cylindrical and flat pores shapes (pancake-shaped) respectively. It worth mentioning that the spherical pores represent the upper bound for the thermal conductivity while the flat pores correspond to the lower bound.

As observed in Fig. 3, our experimental results are in good agreement with the theoretical predictions as they are somewhere between the two limits. However, it can be observed that the thermal conductivity of i) the denser as-sintered specimens are close to the model involving flat shaped pores, ii) the most porous specimens are closer to the model involving spherical pore shapes and iii) the specimens with intermediate densities have intermediate values, lying close to the model involving cylindrical pores.

3.2. Effect of aging on thermal conductivity

Fig. 4 plots the evolution of the thermal conductivity as a function of aging temperature (150 °C, 250 °C and 350 °C), aging time (0 h, 50 h, 200 h and 500 h) and initial porosity i.e. corresponding to the one measured in the as-sintered state (ranging from 25% to 75%).

As observed in Fig. 4, for a given initial porosity, the thermal conductivity increases with aging time but the overall evolution seems independent of the aging temperature i.e. the increase remains relatively

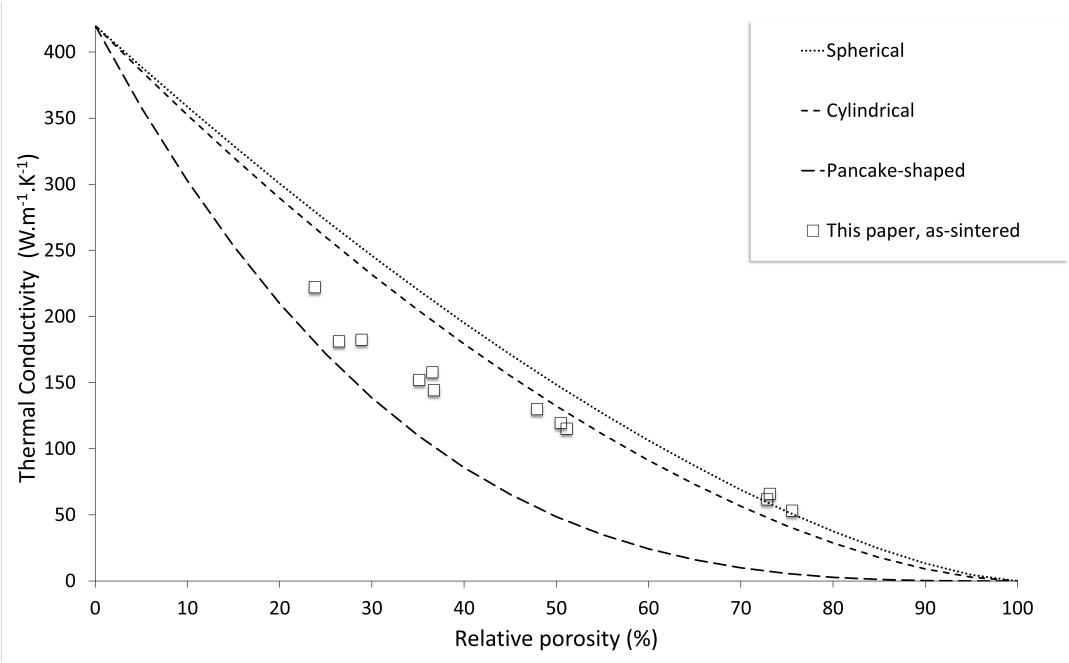

Fig. 3. Thermal conductivity of samples sintered at different pressure with respect to relative porosity (symbols) compared to the theoretical prediction for different pore shapes (lines) [13].

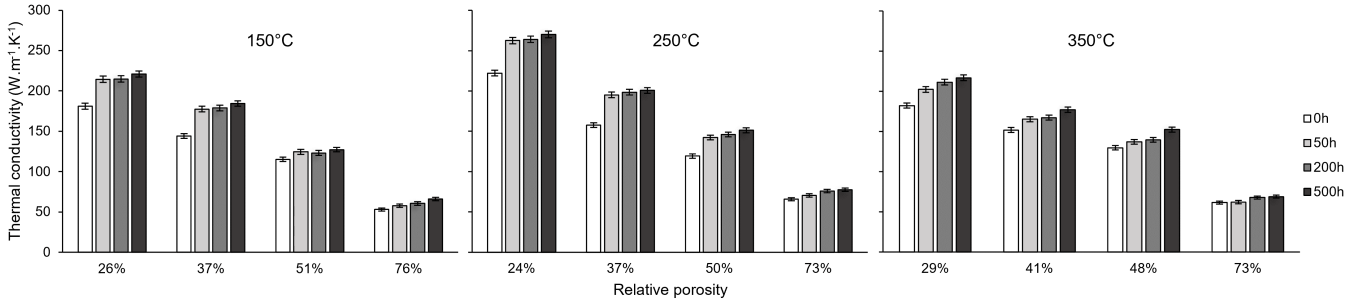

Fig. 4. Thermal conductivities evolution with aging for 0, 50, 200 and 500 h at different temperature 150, 250 and 350 °C.

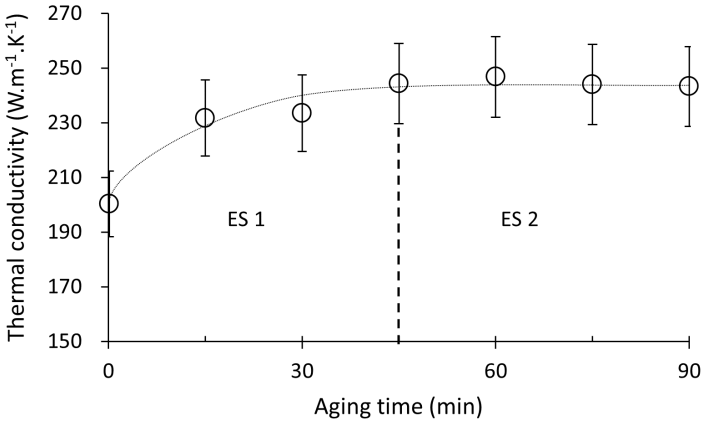

Fig. 5. Determination of ES1 for a specimen sintered under 10 MPa and aged at 150 °C.

constant whatever the aging temperature. Most of the thermal conductivity increase happens within the first 50 h of aging (Evolution Stage 1 - ES1) except for the very porous specimens, elaborated using pressureless sintering (0 MPa). In this latter case, the amount of evolution is limited over the aging time and the evolution itself seems very slow. Interestingly, the thermal conductivity jump observed during ES1 seems directly linked with the applied stress used during sintering: the higher the sintering load (i.e. the lower the porosity), the higher the thermal conductivity jump. However, it must be mentioned that the values found for the specimens sintered at 10 MPa and 5 MPa are very close to each other. This is probably linked with the fact that the initial densities of those specimens are relatively close to each other. In order to monitor the kinetic of ES1, a dedicated specimen was prepared using the highest sintering load and aged at the lowest temperature (150 °C). In this condition, a slower evolution kinetic is expected. As observed in Fig. 5, even at low temperature, the evolution kinetic is relatively fast since the thermal conductivity reaches its maximum within the first 45 minutes (ANOVA Tukey $P_{0-45min} < 0.0001$). Comparing Fig. 4 and Fig. 5 for the same sintering conditions allows to conclude that in fact, the end of ES1 is around 45 minutes at 150 °C for the specimen sintered under 10 MPa. ES1 is expected to be even faster as the aging temperature increases. Beyond ES1, a second evolution stage starts (ES2), during which, qualitatively, only a slight evolution is observed for all the specimens compared to what happened during ES1. When the data are analyzed using the ANOVA Tukey test over the entire aging range (0 h - 500 h), the evolution of the thermal conductivity during ES2 seems significant either for the pressureless sintered specimen ($P_{0MPa} < 0.0001$) and the pressure assisted one ($P_{10MPa} = 0.037$). However, for a given temperature, during ES2, the behavior is nearly identical for all the specimens: the evolution depend neither on the elaboration procedure nor on the density. It must be pointed out that even if the increase of the thermal conductivity is within the same range (a few W/m.K), the values remains remarkably lower for the pressureless specimens than that of the pressure assisted specimens (Fig. 4) hence the lower value of P_{0MPa}. In contrast, while no difference between aging temperatures are observed for shorter aging time (ES1), the amplitude of evolution of the

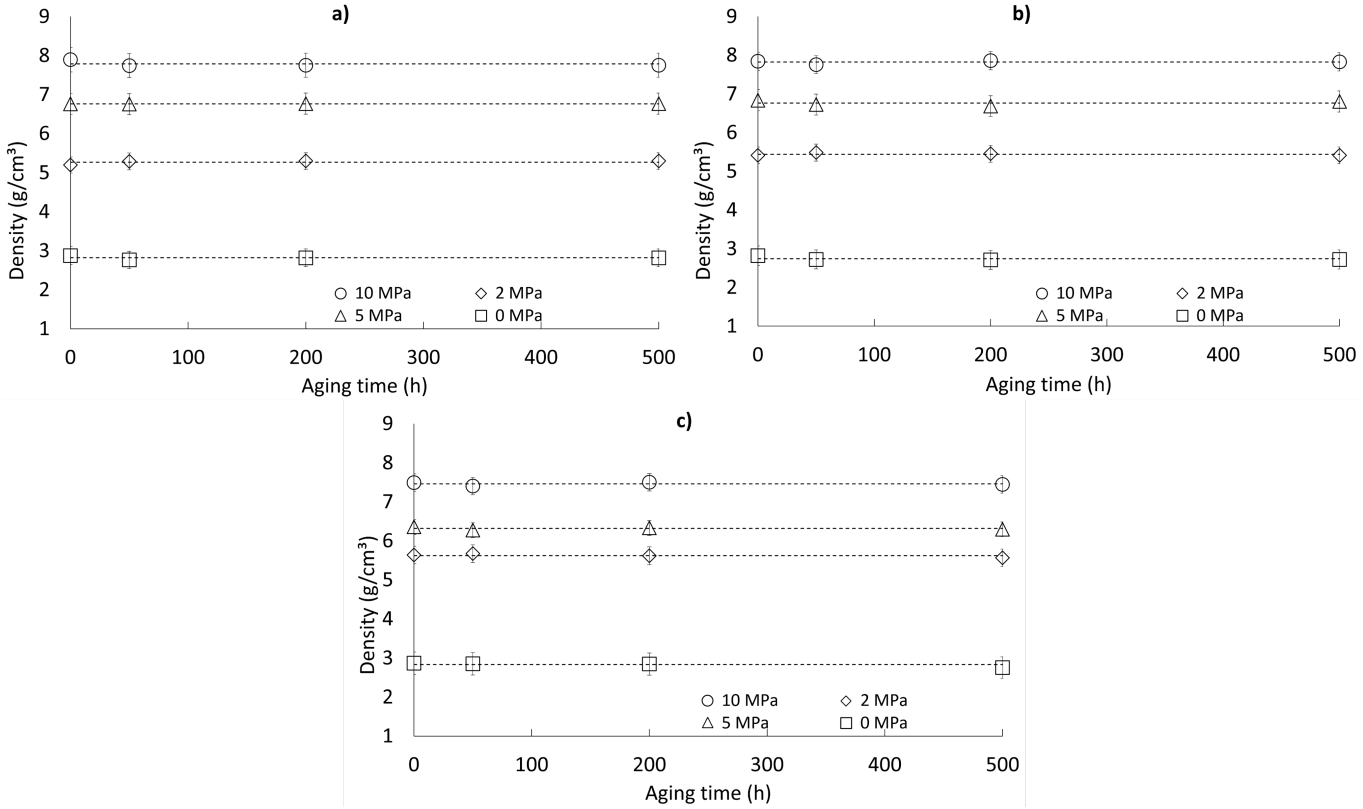

Fig. 6. Relative density evolution of samples sintered at various pressure at different temperature : a) 150, b) 250 and c) 350 °C.

thermal conductivity during ES2 is slightly larger for the specimens aged at 350 °C for 500 h (Fig. 5).

3.3. Density evolution during aging

Microstructure evolution during thermal aging, such as pore volume fraction i.e. densification, grain size growth, may alter the properties of the porous material.

The evolution of the density of sintered Ag during thermal aging (performed after the elaboration process) has been reported in several studies and is still a controversial issue. Some studies reports densitification of the sintered joint during aging while others do not observe this effect. For example, despite a substantial evolution of the porous structure, the pore fraction was reported to remain constant regardless of the aging time and temperature while, some authors report an evolution going from a densification for short aging time followed by a recovery of the initial density after long aging time [4, 8, 21, 39–44]. Most of the studies reporting densification use pore surface fraction analyses based on SEM images of polished surface (2D pore fraction) while those reporting the absence of densitification use either mass/volume ratio, 2D

pore fraction analysis or 3D tomographic images [4, 8, 41, 42, 44]. In the present work, the densities of each specimen were systematically measured before and after each aging step using the mass/volume ratio and, for some of the steps, double checked using 2D pore surface fraction analysis following the protocol described in [3]. Fig. 6 plots the relative densities as a function of sintering conditions, aging temperature and time. As observed qualitatively in Fig. 6, no significant evolution happens even after 500 h spent at 350 °C. This was confirmed for all the aging temperature by ANOVA test between the as-sintered state up to 500h ($P_{150\,^\circ C} = 0.68$, $P_{250\,^\circ C} = 0.17$, $P_{350\,^\circ C} = 0.15$). This is surprising since both aging time and temperature are well over those used during the sintering process but this was already observed using in-situ 3D X-Rays nanotomography [44]. With this observation, it is then possible to plot in the evolution of the thermal conductivity as a function of the density before and after aging and compare it to the model proposed by Miranda-Ordonez [13] (Fig. 7). Compared to the thermal conductivities measured just after sintering, a shift towards higher values is measured for all the specimens but those sintered with no applied load. Interestingly, it is found that the thermal conductivities measured after aging match the theoretical values predicted for both the spherical and cylindrical pores shapes configuration for all of the aged specimens. However, it is worth mentioning that the thermal conductivity measured in the as-sintered state of pressureless specimens were already close to the spherical and cylindrical prediction. As a result, even with the modest evolution observed during ES2, the thermal conductivity of the pressureless sintered specimens stays within the model boundaries.

3.4. Grain size evolution during aging

The average grain size was also carefully monitored during aging at 350 °C, for which the most prominent evolution is expected to take place among all the aging conditions investigated in the present study [39]. Fig. 8 shows an example of the microstructure of a specimen in the as-sintered state (Fig. 8.a, after aging at 350 °C for 200 h Fig. 8.b and after 500 h Fig. 8.c). Table 3 reports the average grain equivalent diameters against aging time for two specimens (sintered at 2 MPa and 10 MPa respectively) as well

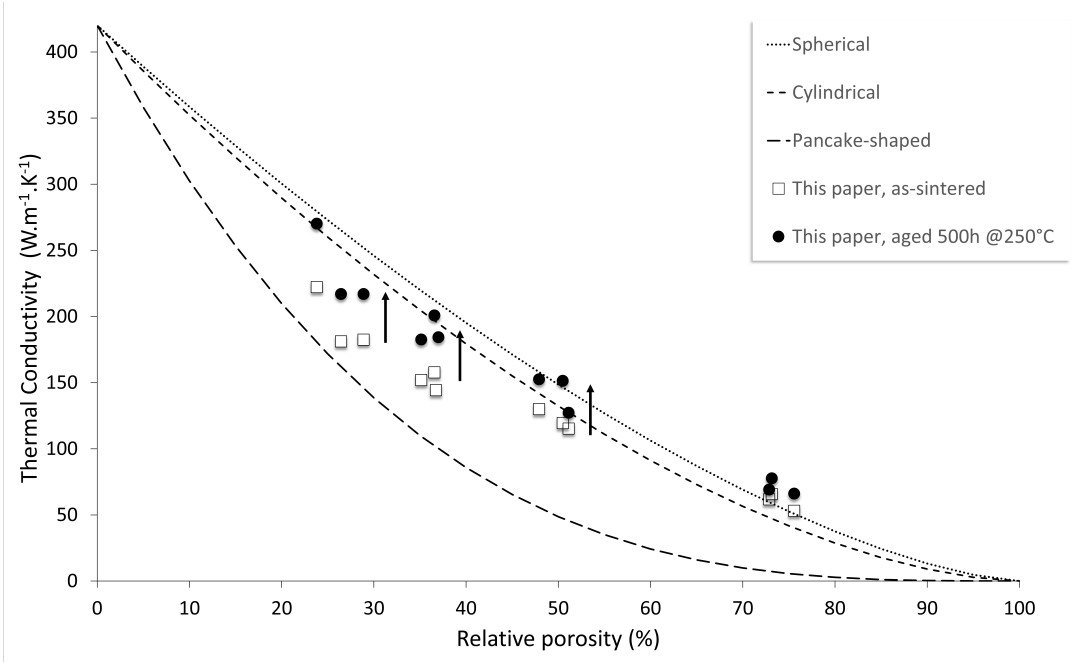

Fig. 7. Thermal conductivity evolution before and after aging for 500 h at 250 °C for Ag sintered under various loads.

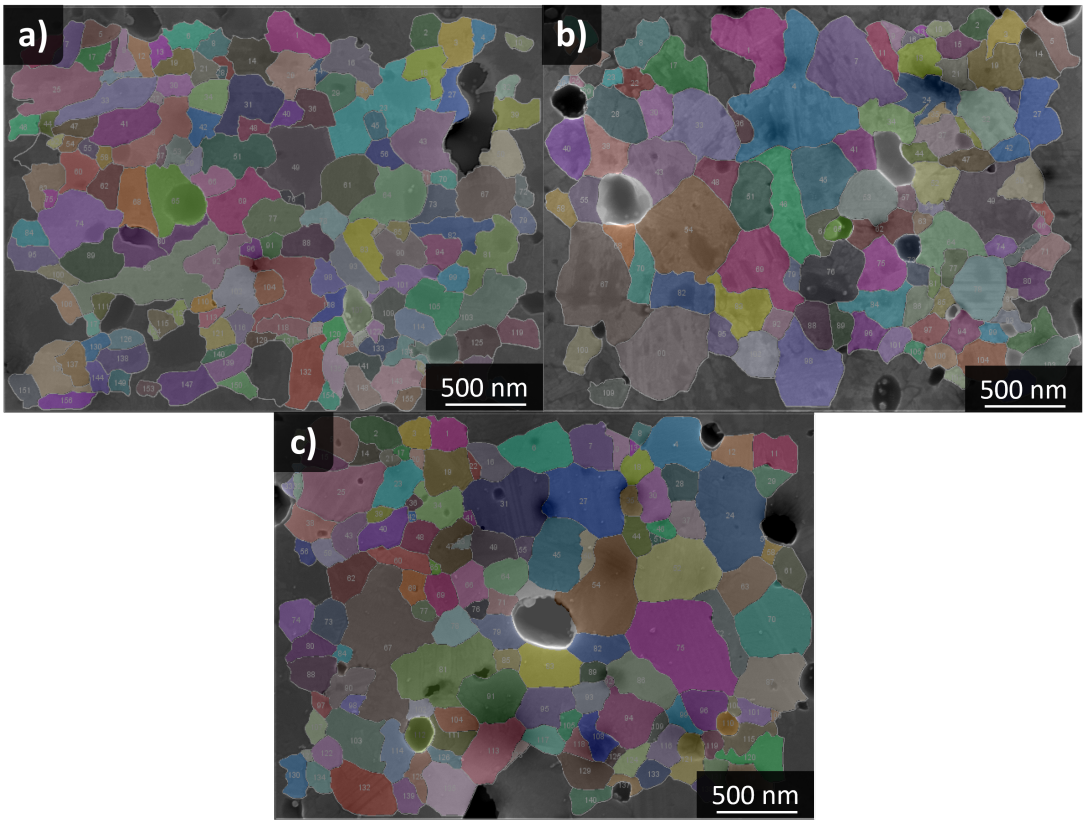

Fig. 8. Ag grains measured by SEM for the 10 MPa sample a) as-sintered, b) after 200 h and c) after 500 h aging time at 350 °C.

Sintering pressure (MPa)	2			10		
Aging Time (h)	0	200	500	0	200	500
Grain size (nm)	301	307	315	295	324	331
Standard deviation (nm)	110	104	101	105	124	124

TABLE 3. Silver grains measured by SEM for the 10MPa as-sintered and aged for 200 h and 500 h at 350 °C samples.

as the corresponding standard deviations. From the data reported in Table 3, the ANOVA and Tukey test show that no significant evolution of the average grain size occurs during aging form 0h to 500h ($P_{2MPa} = 0.98, P_{10MPa} = 0.19$), the average diameter being around 300 nm. This result do not agree with the results reported by Paknejad et al. [39], for which the measurements were based on the evolution of the contact area between sintered Ag and a glass slab observed by optical miscroscopy. However, the present result agree with very long term aging at low temperature (1500 h at 125 °C) previously reported in the literature based on transmission electron microscopy (TEM) measurement [8] and at high temperature (350 °C) by X-rays analysis [45]. In fact, Zuo et al. reported that grain growth takes place only for the first 5 min of the sintering process then stops, even for longer sintering times (20 min) whether at 220 °C or 310 °C [46]. Actually, grain size growth in porous materials is known to be impeded by the presence of numerous pore/grain interfaces, reducing solid-solid contacts. The decrease of contact areas between adjacent grains limits bulk diffusion and grain boundary migration associated with grain growth [22, 23]. Since no significant grain growth was observed even for the highest aging temperature (350 °C), either for specimens sintered with applied loads of 2 MPa or 10 MPa, grain growth is not expected to occur for the other sintering/aging conditions used in the present study since they mostly lead to more porous microstructures.

3.5. Comparison with other estimation methods

The results obtained in this study are compared with results from previous studies (Fig. 9). This literature review is an update to the one proposed by Y. Kim et al. [19]. This comparison also includes the analytical model of Ordonez-Miranda et al. [13]. Because the sintered Ag samples contain a mixture of various pore shapes, the thermal conductivity of the samples should be located between the curve of spherical and

flat shape pores [4, 41, 44]. Values of thermal conductities lying below the flat shape pore model may be biased, as mentioned earlier, by three factor: i) the measurement of density with SEM image analysis, ii) assumptions on heat capacity of Ag and iii) assumptions on interfaces between multiple layers. Both the samples sintering conditions, measurement techniques and results are summarized in Appendix 4. The results were obtained using two different measurement techniques. The first one, consists in placing the sample within a stack of well known materials. This configuration generates thermal contact resistance between the layers that are difficult to estimate, inducing additional uncertainties [13, 17–19]. Other methods, that overcome those thermal contact resistances, require both a contact-less thermal excitation and a temperature measurement, the latest being based on the detection of infrared radiations. Most of the recent thermal conductivity evaluations reported in the literature are based on the original laser flash method which exploits the thermal diffusion in the sample thickness. Those methods are quoted as 1D laser flash method. However, such approaches assume that there is no lateral diffusion, which is probably too strong for super diffusive materials such as Ag. In contrast, the 3D laser flash method used in the present study, takes into account both the in-depth and lateral thermal diffusion. Moreover, real time monitoring of the evolution of the temperature field by high frequency IR camera (1950 Hz), to perform the measurement by means of the ENH estimator increases the reliability and the repeatability.

4. Discussion

As observed in Fig. 4 and Fig. 7, the thermal conductivity is a direct function of the porosity but, for a given initial porosity, its evolution seem independent of the aging temperature and can be divided in two distinct domains: i) ES1 during which a jump in thermal conductivity is observed (it is worth pointing out that the amplitude of the jump is independant of the aging temperature and is proportional to the sintering condition: the larger the sintering load, the denser the specimen, the larger the amplitude of the jump) and ii) ES2 during which the increase is modest except for the tests performed at 350 h. In this latter condition,

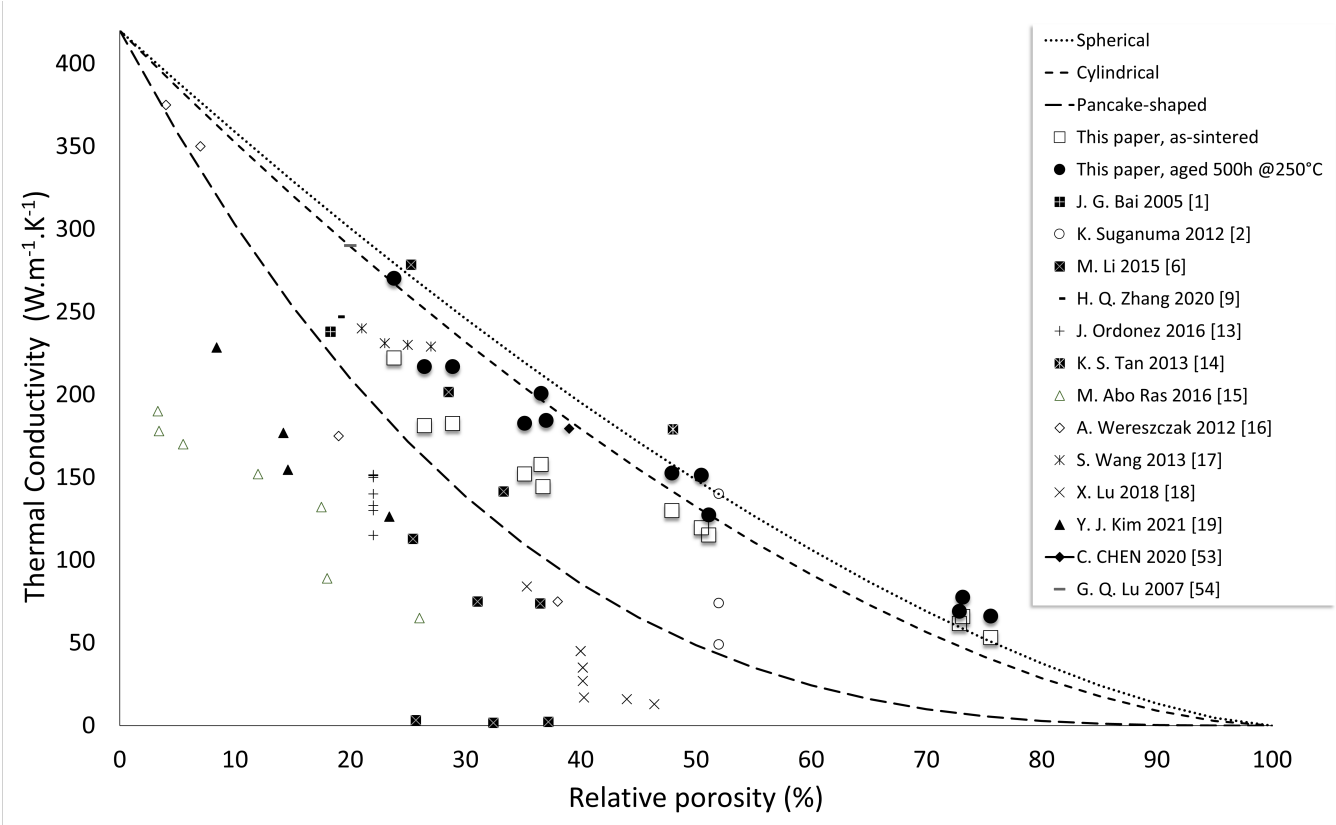

Fig. 9. Thermal conductivity of as-sintered and 500 h aged samples results compared with other studies results and to the theoretical prediction for different pore shapes (lines).

a slightly more noticeable evolution is observed after 500 h whatever the elaboration procedure.

It is well established that thermal transport in materials is influenced by various factors, including porosity, grain size and boundaries, which act as interfaces and reduce the average main free path of carriers such as phonons and electrons, and contribute to the Kapitza resistance [24, 25]. In metals, the heat transfer is derives essentially from the electronic contribution [47]. Since air is not as conductive as solid bulk materials, the presence of pores in a material reduces its thermal conductivity. Since no densification was measured during aging, the evolution of the thermal conductivity observed during ES1 cannot derive from a decrease of the 3D pore fraction within the material. It was reported that pore connectivity arms even more the thermal conductivity of sintered metals by reducing the solid-solid contacts compared to the same material with isolated pores [48, 49]. In the present case, while the pore volume fraction (e.g. density) of sintered Ag remains constant, aging time was shown to favor an increase in pore connectivity following a mechanism well described by Ostwald ripening [4, 41, 44]. Ostwald ripening, based on

diffusion, is a function of the aging temperature: the higher the temperature, the faster the evolution kinetic [41, 44]. According to the literature, the increase of the pore connectivity during aging should result in a decrease of the thermal conductivity, which is not consistent with the observations reported in the present work [48, 49]. However, Carr et al. reported that, after long term aging (1500 h at 125 °C), the pore spatial distribution changes drastically within the material: starting from an initial homogeneous spatial pore distribution in the as-sintered state, it becomes relatively heterogeneous at a micron scale, with highly porous areas (HPA - more solid/pore interfaces - less solid/solid contacts) next to less porous ones (LPA - less solid/pore interfaces - more solid/solid contacts) [4]. Obviously, the local heat transfer at the micrometric scale is expected to be different between HPA and LPA since the local density is different: LPA should exhibit a much higher conductivity compared to HPA. This local effect is likely to be totally averaged in our measurements since these latter are based on the time integration of temperature propagation on the specimen surface after heating using a laser with a spot size within the millimetric range (specimens are 5×5 cm^2). However, the presence of LPA can participate, at least partially to the observed increase in thermal conductivity on the long term. Indeed, according to Fig. 5, the heat conductivity stops evolving massively after a short aging time (ES1) while the evolution of the pore connectivity was reported to increase continuously during aging and the longer the time, the higher the connectivity [4, 44]. While the Ostwald ripening kinetic is closely related to the aging temperature, the thermal conductivity is insensitive to the aging temperature (for a given specimen, the thermal conductivity reaches the same value after a short aging time whatever the temperature (150 °C, 250 °C or 350 °C)). Therefore, the pore evolution cannot account for the fast evolution of the thermal conductivity observed during ES1 (estimated at 45 minutes at 150 °C for the specimen sintered under 10 MPa). As a result, the pore connectivity is unlikely to be responsible for the jump observed during ES1, corresponding to a modest aging time.

Studies have reported a correlation between grain size and heat transfer. Grain boundaries can be seen as sinks for free electrons, resulting in a decrease in both their mean free path and density [45]. As a

result, an increase in grain size leads to a decrease in the number of grain boundaries and an improvement in thermal conductivity [24, 25]. According to Table 3, the grain size remains constant during aging up to 500 h at 350 °C. Therefore, grain growth can be ruled out to explain the thermal conductivity jump observed, especially during ES1. The difference in behavior during ES1 seem to derive directly from the elaboration process. As mentioned earlier, all the specimens were sintered using the same hold time at 270 °C but under different applied load, ranging from 0 MPa to 10 MPa. For a given sintering time, the applied load not only helps densification but was also reported to produce compressive elaboration stresses within free standing specimens [5]. Using dynamic Young's modulus derived from the measurement of the resonance frequency of beams, Milhet et al. [5] showed that the relaxation of the elaboration stresses of free standing Ag joints, sintered at 240 °C under various sintering stresses (5 to 15 MPa), occurred within the first 4 h of aging at 200 °C. For a given density, this resulted in an jump in Young's modulus towards the theoretical value, the higher the compressive stress, the larger the jump [5]. The dependence of the thermal conductivity to stress/strain and dislocation density has been reported in the literature and can even be used to tune the thermal conductivity for some specific applications [26, 50–52]. In the present study, this can help understanding the behavior observed during ES1. No thermal conductivity jump is observed for pressureless sintered specimens (0 MPa), for which no elaboration stresses/strain are expected, while the larger jump is measured for the specimens sintered with the largest applied load i.e. 10 MPa. It is therefore very likely that the elaboration stresses are released and/or dislocation recovery starts during ES1, leading to the progressive evolution of the thermal conductivity towards a stabilized value (Fig. 5), corresponding to the theoretical value (Fig. 6). The evolution of the thermal conductivity during the first 45 minutes of exposure at 150 °C (Fig. 5), is in fact likely to witness the kinetic of the stress release and dislocation network recovery within in the specimen. The kinetic is expected to increase when the aging temperature increases but, once reached, the stabilized value is only a function of the initial porosity but is non-aging temperature dependent.

In the case of sintered Ag, it can be concluded that the compressive stresses resulting from the sintering Ag with an applied load decrease the thermal conductivity at the very beginning of the aging which could be in favor of pressureless sintering. However, since the pore fraction plays the major role on the thermal conductivity, especially after that the elaboration stresses are relaxed, the elaboration conditions (temperature/stress/time) must be finely tuned in order to get the best density/thermal conductivity ratio which would tend to be in favor for a slight sintering pressure or higher sintering temperature to help better densification. The present study also reveals that, for a given density, the optimal thermal properties are obtained only after a small amount of time spent in-operation if sintering is assisted with an applied stress. Once ES1 is finished, ES2 starts, corresponding to a thermal conductivity stabilization and slight evolution with aging time. The increase is more prominent when the temperature is high and the time is very long (between 200 h and 500 h). While no significant grain size growth is observed, evolution of the microstructure in terms of defects (dislocation substructures, grain boundary evolution) might be the driving force for slight thermal conductivity increase [45]. This issue is under current investigation.

5. Conclusion

The thermal conductivity of sintered silver has been measured by a 3D flash method based on ENH estimator. A wide range of densities were obtained using various applied sintering pressure ranging from 0 MPa to 10 MPa, while keeping the sintering time and temperature constant. It is found that the thermal conductivity is closely related to the initial density of the material and evolves rapidly towards a stabilized value during thermal aging. This evolution is insensitive to the aging temperature but only on the initial applied load during sintering. Since the density and the grain size of each specimen were found to remain constant during aging, the evolution of the thermal conductivity results essentially from the release of the elaboration stresses and defects recovery. Since the pore fraction plays the major role on the thermal conductivity, especially after that the elaboration stresses are relaxed, the elaboration conditions

(temperature/stress/time) must be finely tuned in order to get the optimal thermal conductivity for the system.

6. Appendix

Overview of sintered silver thermal conductivity values, including associated process variables and measurement techniques reported by various studies.

TABLE 4. Overview of sintered silver thermal conductivity values, including associated process variables and measurement techniques reported by various studies.

Author	Single layer	Initial particle size (nm)	Sintering T(°C)	Sintering t (min)	Sintering P(MPa)	Dimensions (mm)	Density ($g \cdot cm^{-3}$)	Density Technique	Porosity (%)	Method thermal conductivity	Thermal conductivity ($W.m^{-1}.K^{-1}$)
This paper as-sintered	single layer	20-40	270	5	0	50x50x1.2	2.56	Mass/Volume	76	Flash 3D	54
This paper as-sintered	single layer	20-40	270	5	2	50x50x0.7	5.13	M/V	51	Flash 3D	119
This paper as-sintered	single layer	20-40	270	5	5	50x50x0.5	6.64	M/V	37	Flash 3D	144
This paper as-sintered	single layer	20-40	270	5	10	50x50x0.4	7.72	M/V	26	Flash 3D	185
This paper as-sintered	single layer	20-40	270	5	0	50x50x1.3	2.82	M/V	73	Flash 3D	67
This paper as-sintered	single layer	20-40	270	5	2	50x50x0.7	5.20	M/V	50	Flash 3D	121
This paper as-sintered	single layer	20-40	270	5	5	50x50x0.5	6.66	M/V	37	Flash 3D	161
This paper as-sintered	single layer	20-40	270	5	10	50x50x0.4	8.00	M/V	24	Flash 3D	227
This paper as-sintered	single layer	20-40	270	5	0	50x50x1.4	2.85	M/V	73	Flash 3D	59
This paper as-sintered	single layer	20-40	270	5	2	50x50x0.6	5.47	M/V	48	Flash 3D	133
This paper as-sintered	single layer	20-40	270	5	5	50x50x0.5	6.16	M/V	41	Flash 3D	160
This paper as-sintered	single layer	20-40	270	5	10	50x50x0.5	7.47	M/V	29	Flash 3D	193
Aged @ 150°C 500h	single layer	20-40	270	5	0	50x50x1.2	2.82	M/V	73	Flash 3D	66
Aged @ 150°C 500h	single layer	20-40	270	5	2	50x50x0.7	5.30	M/V	50	Flash 3D	127
Aged @ 150°C 500h	single layer	20-40	270	5	5	50x50x0.5	6.76	M/V	36	Flash 3D	184
Aged @ 150°C 500h	single layer	20-40	270	5	10	50x50x0.4	7.75	M/V	26	Flash 3D	221

Table 4 continued from previous page

Aged @ 250°C 500h	single layer	20-40	270	5	0	50x50x0.13	2.72	M/V	74	Flash 3D	78
Aged @ 250°C 500h	single layer	20-40	270	5	2	50x50x0.7	5.41	M/V	48	Flash 3D	151
Aged @ 250°C 500h	single layer	20-40	270	5	5	50x50x0.5	6.8	M/V	35	Flash 3D	201
Aged @ 250°C 500h	single layer	20-40	270	5	10	50x50x0.4	7.83	M/V	25	Flash 3D	270
Aged @ 350°C 500h	single layer	20-40	270	5	0	50x50x1.4	2.76	M/V	74	Flash 3D	69
Aged @ 350°C 500h	single layer	20-40	270	5	2	50x50x0.6	5.57	M/V	47	Flash 3D	153
Aged @ 350°C 500h	single layer	20-40	270	5	5	50x50x0.5	6.3	M/V	40	Flash 3D	177
Aged @ 350°C 500h	single layer	20-40	270	5	10	50x50x0.5	7.44	M/V	29	Flash 3D	217
H. Zhang 2020 [9]	single layer	110	300	15	3	Diameter12.7x0.5	8.60	-	19	Laser flash (LFA477, Netzsch)	247
J. Ordonez-Miranda 2016 [13]	single layer	Micropaste (Hearus, Inc.)	200	60	5	5x20x0.15	-	SEM	22	LaTIMA	133
Jose Ordonez-Miranda 2016	single layer	Micropaste (Hearus, Inc.)	200	60	5	5x20x0.05	-	SEM	22	LaTIMA	151
M. Abo Ras 2016 [15]	single layer	-	200	-	5	20x5x0.15	-	SEM	26	LaTIMA	65
M. Abo Ras 2016	single layer	-	270	-	5	20x5x0.15	-	SEM	18	LaTIMA	132
M. Abo Ras 2016	single layer	-	200	-	10	20x5x0.15	-	SEM	18	LaTIMA	89
M. Abo Ras 2016	single layer	-	270	-	10	20x5x0.15	-	SEM	12	LaTIMA	152
M. Abo Ras 2016	single layer	-	270	-	15	20x5x0.15	-	SEM	6	LaTIMA	170
M. Abo Ras 2016	single layer	-	270	-	20	20x5x0.15	-	SEM	3	LaTIMA	190

Table 4 continued from previous page

M. Abo Ras 2016	single layer	-	270	-	25	20x5x0.15	-	SEM	3	LaTIMA	178
E. Merten 2015 [12]	single layer	-	250	3	25	-	-	-	-	LaTIMA	258
M. Li 2015 [6]	single layer	-	30	30	0	-	-	Archimedes	32	Laser flash (LFA-457, Netzsch)	2
M. Li 2015	single layer	-	30	30	0	-	-	Archimedes	37	Laser flash (LFA-457, Netzsch)	2
M. Li 2015	single layer	-	30	30	0	-	-	Archimedes	26	Laser flash (LFA-457, Netzsch)	3
M. Li 2015	single layer	-	150	30	0	-	-	Archimedes	36	Laser flash (LFA-457, Netzsch)	74
M. Li 2015	single layer	-	150	30	0	-	-	Archimedes	31	Laser flash (LFA-457, Netzsch)	75
M. Li 2015	single layer	-	150	30	0	-	-	Archimedes	25	Laser flash (LFA-457, Netzsch)	113
M. Li 2015	single layer	50	250	30	0	-	-	Archimedes	33	Laser flash (LFA-457, Netzsch)	142
M. Li 2015	single layer	10	250	30	0	-	-	Archimedes	29	Laser flash (LFA-457, Netzsch)	202
M. Li 2015	single layer	10 + 50	250	30	0	-	-	Archimedes	25	Laser flash (LFA-457, Netzsch)	279
K. S. Tan 2013 [14]	single layer	40 (MTI Corp.)	380	10	10	D12.7x2∼3	-	Archimedes	48	Laser flash (LFA477, Netzsch)	179

Table 4 continued from previous page

A. Wereszczak 2012 [16]	single layer	-	250	10	50	D12.7x2	6.46	M/V	38	Laser flash (TA Instrument)	75
A. Wereszczak 2012	single layer	-	350	10	50	D12.8x2	8.41	M/V	19	Laser flash (TA Instrument)	175
A. Wereszczak 2012	single layer	20μm	350	25	50	D12.9x2	9.66	M/V	7	Laser flash (TA Instrument)	350
A. Wereszczak 2012	single layer	20μm	350	25	50	D12.10x2	10.03	M/V	4	Laser flash (TA Instrument)	375
K. Suganuma 2012 [2]	single layer	8μm + 0.3μm	220	40	-	10x10x1	-	-	52	Laser flash (LFA477, Netzsch)	140
C. CHEN 2020 [53]	Ag/Cu	13	250	30	0	10x10x0.5	-	SEM	39	Laser flash (LFA477, Netzsch)	179
G. Lu 2007 [54]	Ag/Al2O3	-	275	10	0.4	4.3x5.8x5∼8μm	-	SEM	20	Wiedemann-Franz	290
G. Bai 2005 [1]	Ag/Al2O3	1-3μm (C1075, Heraeus Inc.)	280	10	40	-	8.58	Archimede	18	Laser flash	238
Y. Kim 2021 [19]	Cu-Ag-Cu	3μm	200	5	10	D10x2	-	SEM	23	Steady-state (TCM1001, Rhesca)	126
Y. Kim 2021	Cu-Ag-Cu	3μm	250	5	10	D10x2	-	SEM	15	Steady-state (TCM1001, Rhesca)	155
Y. Kim 2021	Cu-Ag-Cu	3μm	300	5	10	D10x2	-	SEM	14	Steady-state (TCM1001, Rhesca)	177

Table 4 continued from previous page

Y. Kim 2021	Cu-Ag-Cu	3µm	350	5	10	D10x2	-	SEM	8	Steady-state (TCM1001, Rhesca)	229
L. Xiuzhen 2018 [18]	sandwich	20	200	30	0	-	5.63	M/V	46	Laser flash	13
L. Xiuzhen 2018	sandwich	20	220	30	0	-	5.88	M/V	44	Laser flash	16
L. Xiuzhen 2018	sandwich	20	260	15	0	-	6.27	M/V	40	Laser flash	17
L. Xiuzhen 2018	sandwich	20	260	20	0	-	6.28	M/V	40	Laser flash	27
L. Xiuzhen 2018	sandwich	20	240	30	0	-	6.28	M/V	40	Laser flash	35
L. Xiuzhen 2018	sandwich	20	260	25	0	-	6.28	M/V	40	Laser flash	35
L. Xiuzhen 2018	sandwich	20	260	30	0	-	6.30	M/V	40	Laser flash	45
L. Xiuzhen 2018	sandwich	20	260	30	0	-	6.30	M/V	40	Laser flash	45
Lu Xiuzhen 2018	sandwich	20	280	30	0	-	6.79	M/V	35	Laser flash	84
S. Wang 2013 [17]	Cu-Ag-Cu	13	200	20	0	1.5x1.5x0.5	-	Archimedes	27	Laser flash (LFA477, Netzsch)	229
S. Wang 2013	Cu-Ag-Cu	13	230	20	0	-	-	Archimedes	25	Laser flash (LFA477, Netzsch)	230
S. Wang 2013	Cu-Ag-Cu	13	250	20	0	-	-	Archimedes	23	Laser flash (LFA477, Netzsch)	231
S. Wang 2013	Cu-Ag-Cu	13	280	20	0	-	-	Archimedes	21	Laser flash (LFA477, Netzsch)	240
K. Suganuma 2012 [2]	Cu-Ag-Cu	8µm + 0.3µm	220	40		10x10x1.5	-	-	52	Laser flash (LFA477, Netzsch)	74

Table 4 continued from previous page

K. Suganuma 2012	DBC substrate	8µm + 0.3µm	240	60	0.07	10x10x0.07	-	-	52	Laser flash (LFA477, Netzsch)	49
J. Ordonez-Miranda 2016 [13]	Si-TIM-Cu	Hearus	200	60	5	Thickness 0.013	-	-	22	Raman thermometry	115
J. Ordonez-Miranda 2016	TIM (Al2O3-Si-Sag-Cu)	Hearus	200	60	5	Thickness 0.013	-	-	22	3\omega	130
J. Ordonez-Miranda 2016	Si-TIM-Cu	Hearus	200	60	5	Thickness 0.013	-	-	22	Raman thermometry	140
J. Ordonez-Miranda 2016	TIM (Al2O3-Si-Sag-Cu)	Hearus	200	60	-	Thickness 0.013	-	-	22	3\omega	150

Acknowledgements

This work received the financial support of the European Union and the Région Nouvelle-Aquitaine through the ERDF fund (EPROM project n°PC-2017-3401110) and the program "transport" of CPER-FEDER 2014-2021. The authors are very grateful to Florence Hamon (Institut Pprime UPR 3346 CNRS) for her help during image acquisition.

References

[1] J. Bai, Z. Zhang, J. Calata, and G.-q. Lu, "Characterization of Low-Temperature Sintered Nanoscale Silver Paste for Attaching Semiconductor Devices", en, in *2005 Conference on High Density Microsystem Design and Packaging and Component Failure Analysis*, Shanghai, China: IEEE, Jun. 2005, pp. 1–5.

[2] K. Suganuma, S. Sakamoto, N. Kagami, D. Wakuda, K.-S. Kim, and M. Nogi, "Low-temperature low-pressure die attach with hybrid silver particle paste", en, *Microelectronics Reliability*, vol. 52, no. 2, pp. 375–380, Feb. 2012.

[3] V. Caccuri, X. Milhet, P. Gadaud, D. Bertheau, and M. Gerland, "Mechanical Properties of Sintered Ag as a New Material for Die Bonding: Influence of the Density", en, *Journal of Elec Materi*, vol. 43, no. 12, pp. 4510–4514, Dec. 2014.

[4] J. Carr, X. Milhet, P. Gadaud, S. A. Boyer, G. E. Thompson, and P. Lee, "Quantitative characterization of porosity and determination of elastic modulus for sintered micro-silver joints", en, *Journal of Materials Processing Technology*, vol. 225, pp. 19–23, Nov. 2015.

[5] X. Milhet, P. Gadaud, V. Caccuri, D. Bertheau, D. Mellier, and M. Gerland, "Influence of the Porous Microstructure on the Elastic Properties of Sintered Ag Paste as Replacement Material for Die Attachment", en, *Journal of Elec Materi*, vol. 44, no. 10, pp. 3948–3956, Oct. 2015.

[6] M. Li, Y. Xiao, Z. Zhang, and J. Yu, “Bimodal Sintered Silver Nanoparticle Paste with Ultrahigh Thermal Conductivity and Shear Strength for High Temperature Thermal Interface Material Applications”, en, *ACS Appl. Mater. Interfaces*, vol. 7, no. 17, pp. 9157–9168, May 2015.

[7] H. Zhang, S. Koga, J. Jiu, S. Nagao, Y. Izumi, E. Yokoi, and K. Suganuma, “Low temperature die attach based on sub-micron Ag particles and the high temperature reliability of sintered joints”, en, in *2015 IEEE 65th Electronic Components and Technology Conference (ECTC)*, San Diego, CA: IEEE, May 2015, pp. 1774–1779.

[8] P. Gadaud, V. Caccuri, D. Bertheau, J. Carr, and X. Milhet, “Ageing sintered silver: Relationship between tensile behavior, mechanical properties and the nanoporous structure evolution”, en, *Materials Science and Engineering: A*, vol. 669, pp. 379–386, Jul. 2016.

[9] H.-Q. Zhang, H.-L. Bai, Q. Jia, W. Guo, L. Liu, and G.-S. Zou, “High Electrical and Thermal Conductivity of Nano-Ag Paste for Power Electronic Applications”, en, *Acta Metall. Sin. (Engl. Lett.)*, vol. 33, no. 11, pp. 1543–1555, Nov. 2020.

[10] G. Bai, “Low-Temperature Sintering of Nanoscale Silver Paste for Semiconductor Device Interconnection”, en, p. 216,

[11] F. Yu, R. W. Johnson, and M. Hamilton, “Pressureless, Low Temperature Sintering of Micro-scale Silver Paste for Die Attach for 300°C Applications”, en, *Additional Conferences (Device Packaging, HiTEC, HiTEN, and CICMT)*, vol. 2014, no. HITEC, pp. 000 165–000 171, Jan. 2014.

[12] E. Merten, T. von Essen, F. Luczack, A. Otto, A. Lunding, P. Lurkens, M. Bast, M. Abo Ras, and S. Rzepka, “Reliability investigation and design of high power rectifier modules based on material characterization, simulation and experimental verification”, en, in *2015 16th International Conference on Thermal, Mechanical and Multi-Physics Simulation and Experiments in Microelectronics and Microsystems*, Budapest, Hungary: IEEE, Apr. 2015, pp. 1–7.

[13] J. Ordonez-Miranda, M. Hermens, I. Nikitin, V. G. Kouznetsova, O. van der Sluis, M. A. Ras, J. Reparaz, M. Wagner, M. Sledzinska, J. Gomis-Bresco, C. Sotomayor Torres, B. Wunderle, and S. Volz, "Measurement and modeling of the effective thermal conductivity of sintered silver pastes", en, *International Journal of Thermal Sciences*, vol. 108, pp. 185–194, Oct. 2016.

[14] Kim Seah Tan and Kuan Yew Cheong, "Physical and Electrical Characteristics of Silver-Copper Nanopaste as Alternative Die-Attach", en, *IEEE Trans. Compon., Packag. Manufact. Technol.*, vol. 4, no. 1, pp. 8–15, Jan. 2014.

[15] M. A. Ras, D. May, J. Heilmann, S. Rzepka, B. Michel, and B. Wunderle, "Processing-structure-property correlations of sintered silver", en, in *2016 15th IEEE Intersociety Conference on Thermal and Thermomechanical Phenomena in Electronic Systems (ITherm)*, Las Vegas, NV, USA: IEEE, May 2016, pp. 1064–1071.

[16] A. A. Wereszczak, D. J. Vuono, H. Wang, M. K. Ferber, and Z. Liang, "Properties of Bulk Sintered Silver As a Function of Porosity", en, Tech. Rep. ORNL/TM-2012/130, 1041433, Jun. 2012, ORNL/TM–2012/130, 1041433.

[17] S. Wang, M. Li, H. Ji, and C. Wang, "Rapid pressureless low-temperature sintering of Ag nanoparticles for high-power density electronic packaging", en, *Scripta Materialia*, vol. 69, no. 11-12, pp. 789–792, Dec. 2013.

[18] X. Lu, W. Ke, C. Zhou, Y. Wu, Q. Zhang, S. Huang, W. Xia, L. Ye, A. Zehri, and J. Liu, "The influence of sintering process on thermal properties of nano-silver paste", en, in *2018 19th International Conference on Electronic Packaging Technology (ICEPT)*, Shanghai: IEEE, Aug. 2018, pp. 1157–1160.

[19] Y.-J. Kim, B.-H. Park, S.-K. Hyun, and H. Nishikawa, "The influence of porosity and pore shape on the thermal conductivity of silver sintered joint for die attach", en, *Materials Today Communications*, vol. 29, p. 102 772, Dec. 2021.

[20] F. Qin, Y. Hu, Y. Dai, T. An, and P. Chen, "Evaluation of thermal conductivity for sintered silver considering aging effect with microstructure based model", en, *Microelectronics Reliability*, vol. 108, p. 113 633, May 2020.

[21] H. Zhang, Z. Zhao, G. Zou, W. Wang, L. Liu, G. Zhang, and Y. Zhou, "Failure analysis and reliability evaluation of silver-sintered die attachment for high-temperature applications", en, *Microelectronics Reliability*, vol. 94, pp. 46–55, Mar. 2019.

[22] J. E. Burke, "Role of Grain Boundaries in Sintering.", en, *J American Ceramic Society*, vol. 40, no. 3, pp. 80–85, Mar. 1957.

[23] R. M. Pasquarelli, J. J. do Rosário, L. Rath, G. A. Schneider, and R. Janssen, "High temperature behavior of monodisperse porosity in alumina films", en, *Journal of the European Ceramic Society*, vol. 35, no. 14, pp. 3917–3926, Nov. 2015.

[24] C.-W. Nan and R. Birringer, "Determining the Kapitza resistance and the thermal conductivity of polycrystals: A simple model", en, *Phys. Rev. B*, vol. 57, no. 14, pp. 8264–8268, Apr. 1998.

[25] H.-S. Yang, G.-R. Bai, L. Thompson, and J. Eastman, "Interfacial thermal resistance in nanocrystalline yttria-stabilized zirconia", en, *Acta Materialia*, vol. 50, no. 9, pp. 2309–2317, May 2002.

[26] H.-F. Lee, S. Kumar, and M. Haque, "Role of mechanical strain on thermal conductivity of nanoscale aluminum films", en, *Acta Materialia*, vol. 58, no. 20, pp. 6619–6627, Dec. 2010.

[27] E. El Rassy, Y. Billaud, and D. Saury, "Simultaneous and direct identification of thermophysical properties for orthotropic materials", en, *Measurement*, vol. 135, pp. 199–212, Mar. 2019.

[28] E. Ruffio, D. Saury, and D. Petit, “Improvement and comparison of some estimators dedicated to thermal diffusivity estimation of orthotropic materials with the 3D-flash method”, en, *International Journal of Heat and Mass Transfer*, vol. 64, pp. 1064–1081, Sep. 2013.

[29] I. Philippi, J. C. Batsale, D. Maillet, and A. Degiovanni, “Measurement of thermal diffusivities through processing of infrared images”, en, *Review of Scientific Instruments*, vol. 66, no. 1, pp. 182–192, Jan. 1995.

[30] J.-C. Krapez, L. Spagnolo, M. Frieß, H.-P. Maier, and G. Neuer, “Measurement of in-plane diffusivity in non-homogeneous slabs by applying flash thermography”, en, *International Journal of Thermal Sciences*, vol. 43, no. 10, pp. 967–977, Oct. 2004.

[31] V. Vavilov, D. Burleigh, and V. Shiryaev, “IR thermographic evaluation of thermal diffusivity anisotropy: Comparative analysis of some algorithms”, en, *Quantitative InfraRed Thermography Journal*, vol. 4, no. 2, pp. 187–200, Dec. 2007.

[32] P. Bison, F. Cernuschi, and E. Grinzato, “In-depth and In-plane Thermal Diffusivity Measurements of Thermal Barrier Coatings by IR Camera: Evaluation of Ageing”, en, *Int J Thermophys*, vol. 29, no. 6, pp. 2149–2161, Dec. 2008.

[33] M. Akoshima and T. Baba, “Study on a Thermal-diffusivity Standard for Laser Flash Method Measurements”, en, *Int J Thermophys*, vol. 27, no. 4, pp. 1189–1203, Jul. 2006.

[34] B. Hay and J.-R. Filtz, “Estimation de l’incertitude de mesure de la diffusivité thermique par méthode flash - Application à cinq matériaux homogènes”, fr, vol. 2008, p. 9,

[35] D. Petit and D. Maillet, “Techniques inverses et estimation de paramètres. Partie 2”, fr, p. 28, 2008.

[36] T. Ishizaki and H. Nagano, “Measurement of 3D thermal diffusivity distribution with lock-in thermography and application for high thermal conductivity CFRPs”, en, *Infrared Physics & Technology*, vol. 99, pp. 248–256, Jun. 2019.

[37] S Touloukian, “Metallic Elements and Alloys”, en, p. 1588,

[38] Y. S. Touloukian and R. W. Powell, “Thermophysical Properties of Matter-The TPRC Data Series. Volume 10. Thermal Diffusivity”, en, vol. Volume 10, p. 757, Jan. 1974.

[39] S. Paknejad, G. Dumas, G. West, G. Lewis, and S. Mannan, “Microstructure evolution during 300 °C storage of sintered Ag nanoparticles on Ag and Au substrates”, en, *Journal of Alloys and Compounds*, vol. 617, pp. 994–1001, Dec. 2014.

[40] S. A. Paknejad, A. Mansourian, J. Greenberg, K. Khtatba, L. Van Parijs, and S. H. Mannan, “Microstructural evolution of sintered silver at elevated temperatures”, en, *Microelectronics Reliability*, vol. 63, pp. 125–133, Aug. 2016.

[41] X. Milhet, A Nait-Ali, and D Tandiang, “Evolution of the nanoporous microstructure of sintered Ag at high temperature using in-situ X-ray nanotomography”, vol. 156, pp. 310–317, Sep. 2018.

[42] Y. Tan, X. Li, G. Chen, Q. Gao, G.-Q. Lu, and X. Chen, “Effects of thermal aging on long-term reliability and failure modes of nano-silver sintered lap-shear joint”, en, *International Journal of Adhesion and Adhesives*, vol. 97, p. 102 488, Mar. 2020.

[43] K. S. Siow and S. T. Chua, “Thermal Ageing Studies of Sintered Micron-Silver (Ag) Joint as a Lead-Free Bonding Material”, en, *Met. Mater. Int.*, vol. 26, no. 9, pp. 1404–1414, Sep. 2020.

[44] K. H. N’Tsouaglo, X. Milhet, J. Colin, L. Signor, A. Nait-Ali, J. Creus, M. Gueguen, P. Gadaud, and M. Legros, “Time-Resolved Evolution of the 3D Nanoporous Structure of Sintered Ag by X-Ray Nanotomography: Role of the Interface with a Copper Substrate”, en, *Adv Eng Mater*, vol. 24, no. 1, p. 2 100 583, Jan. 2022.

[45] X. Qin, B. Wu, Y. Du, L. Zhang, and H. Tang, “An experimental study on thermal diffusivity of nanocrystalline Ag”, en, *Nanostructured Materials*, vol. 7, no. 3, pp. 383–391, Mar. 1996.

[46] Y. Zuo, C. Zhao, A. Robador, M. Wickham, and S. H. Mannan, “Quasi-in-situ observation of the grain growth and grain boundary movement in sintered Cu nanoparticle interconnects”, en, *Acta Materialia*, vol. 236, p. 118 135, Sep. 2022.

[47] C. Kittel, *Introduction to solid state physics*, en, 8th ed. Hoboken, NJ: Wiley, 2005.

[48] C. Vincent, J. Silvain, J. Heintz, and N. Chandra, “Effect of porosity on the thermal conductivity of copper processed by powder metallurgy”, en, *Journal of Physics and Chemistry of Solids*, vol. 73, no. 3, pp. 499–504, Mar. 2012.

[49] A. E. Gheribi, J.-L. Gardarein, F. Rigollet, and P. Chartrand, “Evidence of second order transition induced by the porosity in the thermal conductivity of sintered metals”, en, *APL Materials*, vol. 2, no. 7, p. 076 105, Jul. 2014.

[50] J. N. Lomer and H. M. Rosenberg, “The detection of dislocations by low temperature heat conductivity measurements”, en, *Philosophical Magazine*, vol. 4, no. 40, pp. 467–483, Apr. 1959.

[51] Y.-H. Jeong, M. A. M. Hossain, S.-T. Hong, K.-S. Han, K.-J. Lee, J.-W. Park, and H. N. Han, “Effects of friction stir processing on the thermal conductivity of a strain-hardened Al-Mg alloy”, en, *Int. J. Precis. Eng. Manuf.*, vol. 16, no. 9, pp. 1969–1974, Aug. 2015.

[52] D. S. Nadig, V. Ramakrishnan, P. Sampathkumaran, and C. S. Prashanth, “Effect of cryogenic treatment on thermal conductivity properties of copper”, en, Spokane, Washington, USA, 2012, pp. 133–139.

[53] C. Chen, C. Choe, D. Kim, and K. Suganuma, “Lifetime Prediction of a SiC Power Module by Micron/Submicron Ag Sinter Joining Based on Fatigue, Creep and Thermal Properties from Room Temperature to High Temperature”, en, *Journal of Elec Materi*, vol. 50, no. 3, pp. 687–698, Mar. 2021.

[54] J. G. Bai, T. G. Lei, J. N. Calata, and G.-Q. Lu, “Control of nanosilver sintering attained through organic binder burnout”, en, *J. Mater. Res.*, vol. 22, no. 12, pp. 3494–3500, Dec. 2007.